

Out-of-plane weak ferromagnetism at room temperature in lattice-distortion non-collinear antiferromagnet of single-crystal Mn_3Sn

Bo-Xi Zhang(张博熙), Ping Song(宋平), Shan-Shan Deng(邓珊珊), Li Lou(娄理), and Sen Yao(姚森)
Citation: Chin. Phys. B, 2023, 32 (**8**): 087502. DOI: 10.1088/1674-1056/acca0b
Journal homepage: http://cpb.iphy.ac.cn; http://iopscience.iop.org/cpb

What follows is a list of articles you may be interested in

Topological magnetotransport and electrical switching of sputtered antiferromagnetic $Ir_{20}Mn_{80}$

Danrong Xiong(熊丹荣), Yuhao Jiang(蒋宇昊), Daoqian Zhu(朱道乾), Ao Du(杜奥), Zongxia Guo(郭宗夏), Shiyang Lu(卢世阳), Chunxu Wang(王春旭), Qingtao Xia(夏清涛), Dapeng Zhu(朱大鹏), and Weisheng Zhao(赵巍胜)
Chin. Phys. B, 2023, 32 (**5**): 057501. DOI: 10.1088/1674-1056/acb9ec

Magnetic properties and magnetocaloric effects of $Tm_{1-x}Er_xCuAl$ (x = 0.25, 0.5, and 0.75) compounds

Hao Sun(孙浩), Junfeng Wang(王俊峰), Lu Tian(田路), Jianjian Gong(巩建建), Zhaojun Mo(莫兆军), Jun Shen(沈俊), and Baogen Shen(沈保根)
Chin. Phys. B, 2022, 31 (**12**): 127501. DOI: 10.1088/1674-1056/ac89d8

Magnetic properties and magnetocaloric effect in $RE_{55}Co_{30}Al_{10}Si_5$ (RE = Er and Tm) amorphous ribbons

Hao Sun(孙浩), Junfeng Wang(王俊峰), Lu Tian(田路), Jianjian Gong(巩建建), Zhaojun Mo(莫兆军), Jun Shen(沈俊), and Baogen Shen(沈保根)
Chin. Phys. B, 2022, 31 (**11**): 117503. DOI: 10.1088/1674-1056/ac8733

Process modeling gas atomization of close-coupled ring-hole nozzle for 316L stainless steel powder production

Peng Wang(汪鹏), Jing Li(李静), Hen-San Liu(刘恒三), Xin Wang(王欣), Bo-Rui Du(杜博睿), Ping Gan(甘萍), Shi-Yuan Shen(申世远), Bin Fan(范斌), Xue-Yuan Ge(葛学元), and Miao-Hui Wang(王淼辉)
Chin. Phys. B, 2021, 30 (**5**): 057502. DOI: 10.1088/1674-1056/abd771

Lattice distortion in disordered antiferromagnetic XY models

Li Peng-Fei(李鹏飞) and Cao Hai-Jing(曹海静)
Chin. Phys. B, 2012, 21 (**7**): 077501. DOI: 10.1088/1674-1056/21/7/077501

Out-of-plane weak ferromagnetism at room temperature in lattice-distortion non-collinear antiferromagnet of single-crystal Mn_3Sn

Bo-Xi Zhang(张博熙), Ping Song(宋平)†, Shan-Shan Deng(邓珊珊), Li Lou(娄理), and Sen Yao(姚森)

State Key Laboratory of Metastable Materials Science and Technology and Key Laboratory for Microstructural Material Physics of Hebei Province, School of Science, Yanshan University, Qinhuangdao 066004, *China*

(Received 20 January 2023; revised manuscript received 23 March 2023; accepted manuscript online 4 April 2023)

Out-of-plane weak ferromagnetic (OWFM) spin arrangements with topological properties can realize a series of interesting physical properties. However, this spin structure tends to exist at low temperatures. The OWFM structure can also be induced at room temperature by hydrostatic pressure, whereas this isotropic approach tends to form helical AFM structures. We report the OWFM spin arrangement in single crystal Mn_3Sn by an anisotropic strategy of high-stressconstrained compression deformation at room temperature. Both experimental and theoretical simulation results show that the alignment of the OWFM spin structure is due to the distortion of the atomic scale caused by the strain energy during deformation. The OWFM spin arrangement can significantly change the magnetic property of Mn_3Sn. As a result, the remanent magnetization M_r for the deformed sample (0.056 μ_B/f.u.) is about eleven times that for the pre-deformed sample (0.005 μ_B/f.u.), and the coercivity (H_c) increases from 0 kOe (pre-deformed sample) to 6.02 kOe (deformed sample). Our findings provide a way to generate the OWFM spin structure at room temperature and may give fresh ideas for creating antiferromagnetic materials with excellent physical properties.

Keywords: non-collinear antiferromagnet, high-stress-constrained compression deformation, lattice distortion

PACS: 75.47.Np, 75.30.Gw, 75.50.Ee **DOI:** 10.1088/1674-1056/acca0b

1. Introduction

The non-collinear antiferromagnetic (AFM) configuration with weak ferromagnetism in the strongly correlated Weyl semimetal of Mn_3Sn can spontaneously break the time-reversal symmetry,[1] resulting in plentiful unexpected physical properties in Mn_3Sn, such as anomalous Hall effect,[2–5] spin Hall effect,[6] topological Hall effect,[7] anomalous Nernst and spin Nernst effects,[8,9] terahertz emission,[10] and magneto-optical Kerr effect.[11] These significant properties make Mn_3Sn as one of the most competitive and potential AFM materials in fields of AFM spintronics,[12] spin caloritronics,[13] terahertz devices,[14,15] and so on.

Mn_3Sn has a hexagonal Ni_3Sn-type structure with the $P6_3/mmc$ symmetry and each c-plane consists of a slightly distorted kagome lattice of Mn [Fig. 1(a)].[2] The Mn moments form a chiral 120° triangular AFM ordering with Néel temperature of $\sim$ 420 K.[16,17] Mn_3Sn has an in-plane weak ferromagnetic (IWFM) spin arrangement at room temperature and will derive an out-of-plane weak ferromagnetic (OWFM) spin arrangement with external magnetic field [Fig. 1(b)].[7,18] One of the challenges for Mn_3Sn on its way to application is how to enhance the magnitude of these physical effects in the atmosphere application.[19] The OWFM spin configuration has been confirmed to generate a large anomalous Hall effect in Mn_3Sn owing to its nonvanishing momentum space Berry curvature.[7] Unfortunately, this spin structure tends to exist at low temperatures.[7,18,20] Hydrostatic pressure can induce an OWFM spin configuration at room temperature.[21,22] This isotropic approach also tends to form a helical AFM structure, suppressing the magnitude of the corresponding effects such as the anomalous Hall effect.[22] The anisotropic approach of uniaxial stress has also been applied to the polycrystalline Mn_3Sn by introducing a residual strain.[23] However, this unbounded method can easily crush the polycrystalline bulks and this will greatly reduce its tuning effect on the OWFM spin configuration.

In this article, we report a novel anisotropic strategy to realize the OWFM spin structure by intentionally introducing lattice distortions to drive the Mn moments to line up from in-plane [c-plane, as shown in Fig. 1(a)] to out-of-plane with high-stress constrained compression deformation. The M_s for the deformed sample (0.157 μ_B/f.u.) is about twice the value for the pre-deformed sample (0.068 μ_B/f.u.), the M_r for the deformed sample (0.056 μ_B/f.u.) is about eleven times the value for the pre-deformed sample (0.005 μ_B/f.u.), and the H_c increases from 0 kOe (pre-deformed sample) to 6.02 kOe (deformed sample).

2. Experimental details

Mn_3Sn single crystals were synthesized by the tin-flux growth method.[20] Pieces of Mn (99.98%, Alfa Aesar Corporation) and Sn (99.99%, Alfa Aesar Corporation) were mixed

†Corresponding author. E-mail: psong@ysu.edu.cn

© 2023 Chinese Physical Society and IOP Publishing Ltd

in a molar ratio of Mn : Sn = 7 : 3 and placed in an alumina crucible sealed into a quartz tube under vacuum. The quartz tube was heated to 1000 °C in ten hours. The temperature was slowly cooled to 900 °C at a rate of 1.25 °C/h after maintained for ten hours at 1000 °C. The Mn_3Sn single crystals were then centrifugally separated from the tin flux using an embedded corundum filter. The obtained Mn_3Sn single crystals are in the form of the hexagonal prism with sizable dimensions of $\sim 1.5 \times 1.5 \times 5$ mm^3, as shown in Fig. 1(b). The composition of samples was evaluated by energy-dispersive x-ray (EDX) spectroscopy combined with scanning electron microscopy (SEM) (S-4800, HITACHI). As shown in Fig. 1(c), the EDX measurement reveals the homogeneous distribution of Mn and Sn with a chemical composition of $Mn_{2.98}Sn_{1.02}$ (referred to as Mn_3Sn in the following).

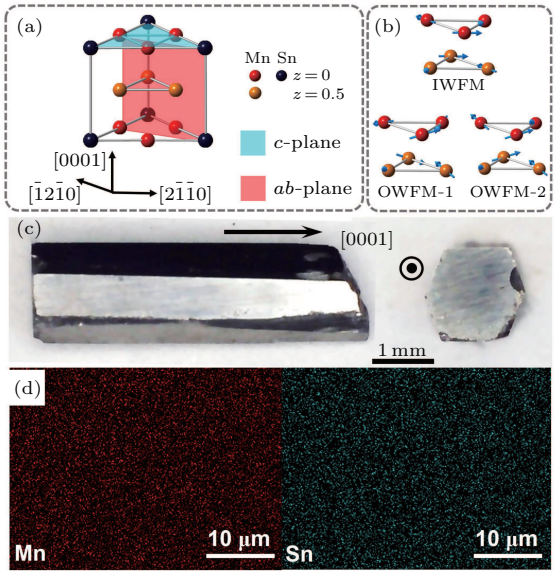


Fig. 1. Non-collinear antiferromagnetism, morphology, and composition of Mn_3Sn single crystals. (a) Schematic crystal structure of Mn_3Sn and its *c*-plane and *ab*-plane. Different colors distinguish the Mn and Sn atoms in planes of $z = 0$ and $z = 0.5$. (b) In-plane weak ferromagnetic (IWFM) and out-of-plane weak ferromagnetic (OWFM) structures of Mn_3Sn. (c) Photos of Mn_3Sn single crystals with indications of crystal orientations. The black arrow and dot indicate [0001]. (d) Element distribution maps of Mn and Sn measured by SEM/EDX.

The deformations were carried out using a commercial 600 kN machine. The sliced Mn_3Sn single crystals were sealed into the steel capsule and then underwent a high-stress compression deformation. For details of the deformation, please refer to Ref. [24]. The crystal structure and microstructure of samples were characterized by x-ray diffraction (XRD) with Co K_α radiation (PIXcel-3D, PANalytical B.V., Inc.) and transmission electron microscopy (TEM) (JEM-2100 Plus, JEOL). The Rietveld refinements were performed with a commercial software (PANalytical B.V., Inc.). The magnetic measurements were achieved using a physical property measurement system (PPMS-9, Quantum Design).

3. Results and discussion

Figure 2 shows the crystal structures of Mn_3Sn with orientations of [0001] and [11$\bar{2}$0] before and after the deformation process. The XRD results [Figs. 2(a) and 2(b)] and the selected area electron diffraction (SAED) results [Fig. 2(g)] indicate high-quality single crystals of the as-prepared Mn_3Sn (referred to as S1 and S2 below). The Rietveld fitting results show the $P6_3/mmc$ symmetry with lattice-parameter ratios of $c/a = 0.800$ and microstrain of $\alpha = 0.22$ % for S1 and $\alpha = 0.51\%$ for S2 (as listed in Table 1). The microstrain α is defined as the deviation between the crystal spacing and its ideal value. The value of α can be calculated with

$$\alpha = \frac{|B_{\text{obs.}} - B_{\text{std.}}|}{4 \tan \theta},$$

where $B_{\text{obs.}}$ is the full width at half maximum (FWHM) of the measured sample, $B_{\text{std.}}$ is the FWHM of the instrument, and θ is the diffraction angle. The emerging microstrain in S1 and S2 may be due to the occurrence of dislocations [Fig. 2(h)] during the molten-metal flux growth process.[25]

Both the as-prepared samples of S1 and S2 then undergo a high-stress compression deformation process with stress ($\sim$ 2 GPa) parallel to [0001] for S1 and parallel to [11$\bar{2}$0] for S2. There are three main characteristics in the XRD results of DS1 and DS2. First of all, the deformed S1 and S2 (referred to as DS1 and DS2 below, respectively) still retain their original textures [Fig. 2(c) and 2(d)] with a slight crystal slip [Fig. 2(i)]. The ratio of $I_{(0002)}/I_{(0004)}$ is 27.0 for S1 and 13.1 for DS1. The ratio of $I_{(11\bar{2}0)}/I_{(22\bar{4}0)}$ is 1.8 for S2 and 0.5 for DS2. This result indicates that during the deformation process, the intensity of diffraction peaks at lower diffraction angles [(0002) and (11$\bar{2}$0)] decreases more obviously than that of higher diffraction angles [(0004) and (22$\bar{4}$0)]. The intensity decrease of diffraction peaks after deformation may come from the weakening of crystal orientation due to slight crystal-plane slip during the deformation process,[26] and the diffraction peaks with large lattice spacing [(0002) and (11$\bar{2}$0)] are more likely to be destroyed by slip. Secondly, the FWHM of the (0002) peak decreases significantly with stress [Fig. 2(e)], indicating a decrease of the microstrain α in DS1. The decrease of α comes from the inhibition of dislocations by deformation stress. The inhibition of the dislocation is irreversible. This is due to the fact that the deformation of the sample is irreversible.

Thirdly, as shown in Figs. 2(e) and 2(f), the peak positions shift to a higher degree with stress, indicating the lattice distortions in DS1 and DS2. As a result, the fitted c/a for DS1 decreases from 0.800 to 0.796, and the fitted c/a for DS2 increases from 0.800 to 0.804 (Table 1). In detail, the compression deformation parallel to [0001] in DS1 reduces the lattice parameter of c and stretches a, and the compression deformation parallel to [11$\bar{2}$0] in DS2 inversely stretches c and reduces

a. This anisotropic strainenergy-induced lattice distortion will affect the exchange coupling between the Mn moments in the same planes and the adjacent planes.[27,28]

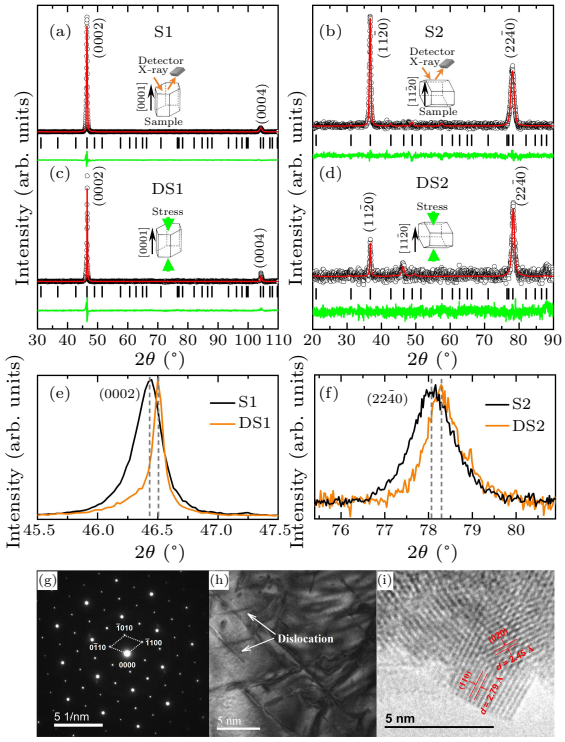


Fig. 2. Crystal structures of single-crystal Mn_3Sn before and after the deformation process. XRD patterns of (a) the as-prepared Mn_3Sn (S1) measured perpendicular to (0001), (b) the as-prepared Mn_3Sn (S2) measured perpendicular to $(11\bar{2}0)$, (c) the deformed Mn_3Sn (DS1) measured perpendicular to (0001), and (d) the deformed Mn_3Sn (DS2) measured perpendicular to $(11\bar{2}0)$. Insets show the schematic illustration of the XRD measurement and the stress direction. Circles show the experimental intensities ($I_{obs.}$), the red solid line shows the calculated intensities ($I_{calc.}$), the green solid line is the difference of $I_{obs.} - I_{calc.}$, and the vertical lines indicate the angular positions of the Bragg reflections. (e) Enlarged view of (0002) peaks in the S1 and DS1 samples. (f) Enlarged view of $(22\bar{4}0)$ peaks in the S2 and DS2 samples. (g) SAED pattern of S1. (h) TEM image of S1. (i) High-resolution TEM image of DS2.

Table 1. Rietveld refinement results of single-crystal Mn_3Sn before and after the deformation process. Here, f is the goodness of fit, R_p the profile R value, R_{wp} the weighted profile R value, a and c the lattice parameters, and α the microstrain parameter.

Sample	S1	DS1	S2	DS2
f	1.59	1.46	0.95	0.87
R_p	5.22	3.77	3.38	2.94
R_{wp}	7.41	5.61	4.30	3.65
a (Å)	–	–	5.683	5.654↓
c (Å)	4.537	4.529 ↓	–	–
α (%)	0.22	0.02	0.51	0.09

To test this scenario, we performed magnetic anisotropy measurements. Figure 3 shows the field dependence of the magnetization M for S1 and DS1 in the magnetic fields $H//[0001]$ and $H\perp[0001]$. The hysteresis loops cannot saturate even at a magnetic field of $H = 28$ kOe because of the AFM domains with strong anisotropy in S1 and DS1.

As shown in Fig. 3, for $H//[0001]$, there is no significant change in the hysteresis loop of DS1 compared to S1, while for $H\perp[0001]$, the hysteresis loop of DS1 changes significantly. The remanent magnetization (M_r) increases from 0.005 μ_B/f.u. to 0.021 μ_B/f.u., and the H_c increases from 0.29 kOe to 3.94 kOe [Fig. 3(b)]. This phenomenon may be caused by the anisotropic compression deformation parallel to [0001] in DS1. This anisotropic strain energy reduces the lattice parameter of c and stretches a, thus deriving the OWFM spin structure.

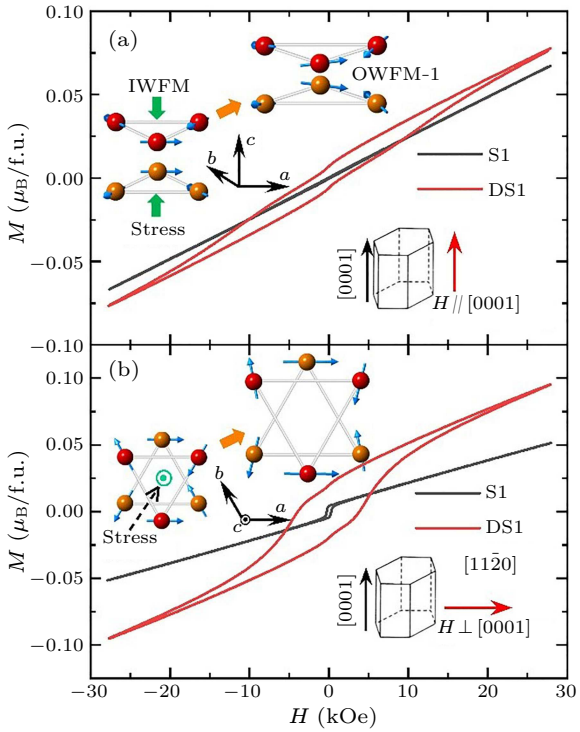


Fig. 3. Enhanced in-plane weak ferromagnetism in Mn_3Sn. (a) Hysteresis loops of the S1 and DS1 samples in the magnetic field $H//[0001]$. (b) Hysteresis loops of the S1 and DS1 samples in the magnetic field $H\perp[0001]$. The upper left insets in (a) and (b) indicate the magnetic structures before and after deformation, respectively. Red and orange spheres indicate the Mn atoms, and different colors are used to distinguish those in the different planes. The bottom insets on the right in panels (a) and (b) show the schematic illustrations of the magnetic measurements.

Figure 4 shows the field dependence of the magnetization M for S2 and DS2 in $H//[0001]$ and $[11\bar{2}0]$. The magnetic properties of DS2 are significantly enhanced compared with DS1. The out-of-plane M_r of DS2 increases from 0 μ_B/f.u. to 0.043 μ_B/f.u., and H_c increases from 0 kOe to 6.02 kOe [Fig. 4(a)]. The in-plane M_r increases from 0.005 μ_B/f.u. to 0.056 μ_B/f.u., and the coercivity (H_c) increases from 0.29 kOe to 3.44 kOe [Fig. 4(b)]. The significant enhancement of the magnetic properties may stem from the slight crystal slip[29] and the distortion of the crystal structure, where the compression deformation parallel to $[11\bar{2}0]$ in DS2 stretches the lattice constant c and reduces a. In short, whether the value of c/a increases or decreases, the spin structure of OWFM can be deduced to enhance the magnetic properties of the sample. However, from the present results, increasing the value of c/a can better enhance the magnetic properties of single-crystal Mn_3Sn.

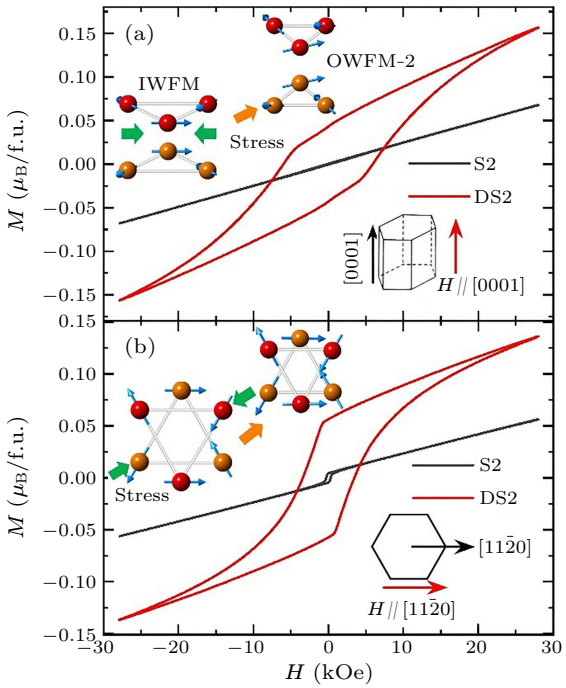


Fig. 4. Out-of-plane and in-plane weak ferromagnetism in Mn_3Sn. (a) Hysteresis loops of the S2 and DS2 samples in the magnetic field $H//[0001]$. (b) Hysteresis loops of the S2 and DS2 samples in the magnetic field $H//[11\bar{2}0]$. The upper left insets in panels (a) and (b) indicate the magnetic structures before and after deformation, respectively. Red and orange spheres indicate the Mn atoms and different colors are used to distinguish those in the different planes. The bottom right insets in panels (a) and (b) show the schematic illustrations of the magnetic measurements.

To understand the effect of strain energy on the configuration of the OWFM spin structure, we performed Monte Carlo simulations using the following minimal Heisenberg Hamiltonian[30]

$$\mathcal{H} = \sum_{ij} J_{ij}\widehat{\boldsymbol{S}}_i \cdot \widehat{\boldsymbol{S}}_j + D\sum_{\langle i,j\rangle} \widehat{\boldsymbol{z}} \cdot (\widehat{\boldsymbol{S}}_i \times \widehat{\boldsymbol{S}}_j) + K\sum_i (\widehat{\boldsymbol{n}}_i \cdot \widehat{\boldsymbol{S}}_i)^2, \quad (1)$$

where J_{ij} is the exchange constant between the spins $\boldsymbol{S}_i$ and $\boldsymbol{S}_j$, D is the Dzyaloshinskii–Moriya (DM) interaction constant, K is the anisotropy constant, and $\boldsymbol{n}_i$ represents the local anisotropy axis. The first term denotes the usual isotropic exchange interaction, the second term is the DM interaction between Mn atom and its nearest neighbor, while the last term denotes a single-ion anisotropy related to the local easy axes on the *ab* plane, respectively.[30]

It has been confirmed that the uniaxial strain in the kagome antiferromagnet Mn_3Sn can produce an extra easy-axis anisotropy which can be used to control the magnetic ground state.[31] The strains in our case are of two types: in-plane shear $\varepsilon_{xx} - \varepsilon_{yy}$, ε_{xy} and out-of-plane shear ε_{xz}, ε_{yz}. We use a tensor $\varepsilon_{ij} = (\partial_i u_j + \partial_j u_i)$ to represent the uniaxial strain with $\boldsymbol{u}$ representing the displacement field on the lattice. Since the order is set by the Heisenberg exchange with $J \gg D \gg K$,[31] we just verify the effect of strain on the first term in Eq. (1) to simplify the simulating process. The effect of strain in Hamiltonian (1) is presented as[31]

$$\sum_{ij}\left[\frac{\partial J}{\partial \widehat{\boldsymbol{u}}} \cdot \delta\widehat{\boldsymbol{u}}\right]\widehat{\boldsymbol{S}}_i \cdot \widehat{\boldsymbol{S}}_j. \quad (2)$$

The corresponding value of J during the simulating process refers to Ref. [30] and the simulated result is illustrated in Fig. 5. As shown in Fig. 5, the spin arrangement of Mn moments has a transition from IWFM to OWFM under uniaxial strains. This calculation result indicates that the uniaxial strain energy can trigger the formation of OWFM spin configuration by the displacement field acting on the exchange interaction.

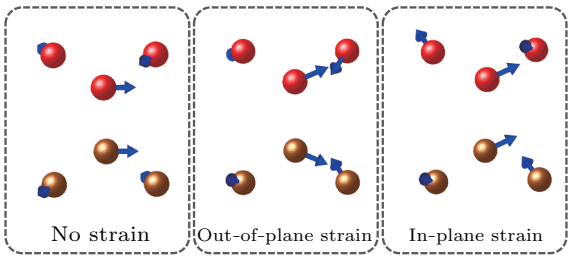


Fig. 5. Simulated spin structures of Mn_3Sn under different uniaxial strains. (a) Spin structure with no strain. (b) Spin structure with the out-of-plane strain. (c) Spin structure with the in-plane strain. Red and orange spheres indicate the Mn atoms and different colors are used to distinguish those in the different planes. Blue arrows indicate the direction of the Mn moments.

We conclude that the anisotropic deformation strategy leads to atomic-scale distortion. Such an anisotropic distortion affects the exchange coupling between Mn moments in the same and adjacent planes, resulting in an out-of-plane arrangement of weak ferromagnetic moments. The efficacy of the anisotropic severe plastic deformation technique has also been demonstrated in creating high-performance permanent-magnet materials and antiferromagnetic materials.[32–42]

4. Conclusion

In summary, we have realized the OWFM spin structure by intentionally introducing lattice distortion to drive the Mn moments to line up from in-plane to out-of-plane with anisotropic high-stress compression deformation. Both experimental and theoretical simulation results show that the alignment of the OWFM spin structure is due to the distortion of the atomic scale caused by the strain energy during the deformation. High magnetic properties are obtained when the stress parallels to $[11\bar{2}0]$. The M_r for the deformed sample (0.056 μ_B/f.u.) is about eleven times the value for the pre-deformed sample (0.005 μ_B/f.u.) ($H//[11\bar{2}0]$), and the H_c increases from 0 kOe (pre-deformed sample) to 6.02 kOe (deformed sample) ($H//[0001]$). We find that anisotropic high-stress compression deformation is an effective way to induce the OWFM spin structure, which may provide new ideas for research of antiferromagnetic materials in applications of spintronic devices.

Acknowledgments

This work was supported by the National Natural Science Foundation of China (Grant Nos. 52101233 and 52071279), the Hebei Natural Science Foundation (Grant No. E2022203010), the China Postdoctoral Science Foundation (Grant No. 2022M712685), and the Innovation Capability Improvement Project of Hebei Province (Grant No. 22567605H).

References

[1] Kuroda K, Tomita T, Suzuki M T, Bareille C, Nugroho A A, Goswami P, Ochi M, Ikhlas M, Nakayama M, Akebi S, Noguchi R, Ishii R, Inami N, Ono K, Kumigashira H, Varykhalov A, Muro T, Koretsune T, Arita R, Shin S, Kondo T and Nakatsuji S 2017 *Nat. Mater.* **16** 1090
[2] Nakatsuji S, Kiyohara N and Higo T 2015 *Nature* **527** 212
[3] Ikeda T, Tsunoda M, Oogane M, Oh S, Morita T and Ando Y 2018 *Appl. Phys. Lett.* **113** 222405
[4] Higo T, Qu D, Li Y, Chien C L, Otani Y and Nakatsuji S 2018 *Appl. Phys. Lett.* **113** 202402
[5] You Y, Chen X, Zhou X, Gu Y, Zhang R, Pan F and Song C 2019 *Adv. Electron. Mater.* **5** 1800818
[6] Zhang Y, Sun Y, Yang H, Železný J, Parkin S P P, Felser C and Yan B 2017 *Phys. Rev. B* **95** 075128
[7] Rout P K, Madduri P V P, Manna S K and Nayak A K 2019 *Phys. Rev. B* **99** 094430
[8] Guo G Y and Wang T C 2017 *Phys. Rev. B* **96** 224415
[9] Li X, Xu L, Ding L, Wang J, Shen M, Lu X, Zhu Z and Behnia K 2017 *Phys. Rev. Lett.* **119** 056601
[10] Zhou X, Song B, Chen X, You Y, Ruan S, Bai H, Zhang W, Ma G, Yao J, Pan F, Jin Z and Song C 2019 *Appl. Phys. Lett.* **115** 182402
[11] Higo T, Man H, Gopman D B, Wu L, Koretsune T, van't Erve O M J, Kabanov Y P, Rees D, Li Y, Suzuki M T, Patankar S, Ikhlas M, Chien C L, Arita R, Shull R D, Orenstein J and Nakatsuji S 2018 *Nat. Photon.* **12** 73
[12] Jungwirth T, Marti X, Wadley P and Wunderlich J 2016 *Nat. Nanotechnol.* **11** 231
[13] Bauer G E W, Saitoh E and van Wees B J 2012 *Nat. Mater.* **11** 391
[14] Ferguson B and Zhang X C 2002 *Nat. Mater.* **1** 26
[15] Tonouchi M 2007 *Nat. Photon.* **1** 97
[16] Nagamiya T 1979 *J. Phys. Soc. Jpn.* **46** 787
[17] Tomiyoshi S and Yamaguchi Y 1982 *J. Phys. Soc. Jpn.* **51** 2478
[18] Tomiyoshi S, Abe S, Yamaguchi Y, Yamauchi H and Yamamoto H 1986 *J. Magn. Magn. Mater.* **54** 1001
[19] Muduli P K, Higo T, Nishikawa T, Qu D, Isshiki H, Kondou K, Nishio-Hamane D, Nakatsuji S and Otani Y 2019 *Phys. Rev. B* **99** 184425
[20] Sung N H, Ronning F, Thompson J D and Bauer E D 2018 *Appl. Phys. Lett.* **112** 132406
[21] Lingannan G, Singh A K, Joseph B, Singh S and Arumugam S 2021 *Phys. Status Solidi RRL* **15** 2000605
[22] Singh C, Singh V, Pradhan G, Srihari V, Poswal H K, Nath R, Nandy A K and Nayak A K 2020 *Phys. Rev. Res.* **2** 043366
[23] Deng J J, Zhao M Y, Wang Y, Wu X, Niu X T, Ma L, Zhao D W, Zhen C M and Hou D L 2022 *J. Phys. D: Appl. Phys.* **55** 275001
[24] Song P, Yao S, Zhang B, Jiang B, Deng S, Guo D, Ma L and Hou D 2022 *Appl. Phys. Lett.* **120** 192401
[25] Tachibana M 2017 *Beginner's Guide to Flux Crystal Growth* (Tokyo: Springer) pp. 9–20
[26] Wei P T, Lu C, Tieu K, Su L H, Deng G Y and Huang W B 2017 *Mater. Sci. Eng. A* **684** 239
[27] Hong W, Liu L, Liu C, Ma X, Koda A, Li X, Song J, Yang W, Yang J, Cheng P, Zhang H, Bao W, Ma X, Chen D, Sun K, Guo W, Luo H, Sandvik A W and Li S 2021 *Phys. Rev. Lett.* **126** 037201
[28] Hou Y S, Xiang H J and Gong X G 2015 *Sci. Rep.* **5** 13159
[29] Kandra J T, Lee J Y and Pope D P 1991 *Mater. Sci. Eng. A* **145** 189
[30] Park P, Oh J, Uhlířová K, Jackson J, Deák A, Szunyogh L, Lee K H, Cho H, Kim H L, Walker H C, Adroja D, Sechovsky V and Park J G 2018 *npj Quantum Mater.* **3** 63
[31] Dasgupta S 2022 *Phys. Rev. B* **106** 064431
[32] Li X, Lou L, Song W, Huang G, Hou F, Zhang Q, Zhang H T, Xiao J, Wen B and Zhang X Y 2017 *Adv. Mater.* **29** 1606430
[33] Huang G, Li X, Lou L, Hua Y, Zhu G, Li M, Zhang H T, Xiao J, Wen B, Yue M and Zhang X Y 2018 *Small* **14** 1800619
[34] Zhang X Y 2020 *Mater. Res. Lett.* **8** 49
[35] Li X, Lou L, Song W, Zhang Q, Huang G, Hua Y, Zhang H T, Xiao J, Wen B and Zhang X Y 2017 *Nano Lett.* **17** 2985
[36] Lou L, Li Y, Li X, Li H, Li W, Hua Y, Xia W, Zhao Z, Zhang H, Yue M and Zhang X Y 2021 *Adv. Mater.* **33** 2102800
[37] Zhang H T and Zhang X Y 2022 *Mater. Res. Lett.* **10** 1
[38] Liu Y, Xu L, Wang Q, Li W and Zhang X Y 2009 *Appl. Phys. Lett.* **94** 172502
[39] Li W, Li L, Nan Y, Li X, Zhang X Y, Gunderov D V, Stolyarov V V and Popov A G 2007 *Appl. Phys. Lett.* **91** 062509
[40] Li H, Lou L, Hou F, Guo D, Li W, Li X, Gunderov D V, Sato K and Zhang X Y 2013 *Appl. Phys. Lett.* **103** 142406
[41] Li W, Li L L, Nan Y, Xu Z, Zhang X Y, Popov A G, Gunderov D V and Stolyarov V V 2008 *J. Appl. Phys.* **104** 023912
[42] Zhang H T, Zhang T and Zhang X Y 2023 *Adv. Sci.* **10** 2300193